Electronic Supplementary Information

Concave Bi_2WO_6 nanoplates with oxygen vacancies achieving enhanced electrocatalytic oxygen evolution in near-neutral water

Zhu-Ping Nie, [a] De-Kun Ma, *[a] Guo-Yong Fang, [ab] Wei Chen [a] and Shao-Ming Huang *[a]

[a]*Nanomaterials and Chemistry Key Laboratory, Wenzhou University, Wenzhou, Zhejiang 325027, P. R. China*

[b]*National Laboratory of Solid State Microstructures, College of Engineering and Applied Sciences, Nanjing University, Nanjing 210093, China*

Experimental section

Synthesis of rod-like Bi_2O_3. Rod-like Bi_2O_3 was synthesized according to previous report.[1] In a typical experimental procedure, 4 mmol of $Bi(NO_3)_3 \cdot 5H_2O$ was dissolved in 25 mL of dilute HNO_3 solution (containing 10 mL of 70% HNO_3) with addition of 2 mL of aqueous polyvinyl alcohol solution (PVA 17–88, 2.5 wt%). The obtained mixtures were stirred until they became a transparent solution. Then, 15 mL of 0.1 g mL^- NaOH solution was added into this solution drop by drop over 30 min under an ice water bath and intensively stirring condition. The white precipitates formed gradually. The whole mixture was then stirred for another 30 min, and then, the white suspension was heated at room for 2 h without stirring. The final yellow products were collected and washed with hot distilled water and absolute ethanol for several times and then dried at 60 °C under vacuum.

Synthesis of $W_{18}O_{49}$ nanowires. The synthesis of $W_{18}O_{49}$ nanowires followed previous report.[2] In a typical procedure, 0.5 g of WCl_6 was put in 100 mL of absolute ethanol, and a transparent yellow solution was formed. The obtained transparent yellow solution was then transferred to a Teflon-lined stainless steel autoclave and heated at 180 °C for 24 h. The final blue flocculent

precipitate was collected, washed with distilled water and absolute ethanol in turn, and dried in vacuum at 60 °C.

Synthesis of Bi_2WO_6 nanoplates. The synthesis of Bi_2WO_6 nanoplates is in line with the reference.[3] In a typical procedure, 1 mmol of $Bi(NO_3)_3 \cdot 5H_2O$ was added to 1 M HNO_3 to form a clear solution under stirring for 30 min at room temperature. Afterward, 25 mL of solution contained 0.5 mmol of $Na_2WO_4 \cdot 2H_2O$ and 1 mL of oleylamine was added into the above solution. The pH value of the suspension was adjusted to *ca*. 7 with $NH_3 \cdot H_2O$. The mixture was finally transferred into a 50 mL Teflon-lined autoclave and maintained at 200 °C for 20 h. The reactor was cooled to room temperature naturally. The resultant products were collected and washed several times with acetone and deionized water and dried at 60 °C in air.

Calculations of adsorption energy. The Bi_2WO_6 (010) surface was cleaved from Russellite crystal with space group *B*2*cb*.[1] The slab thickness was approximately 8.0 Å. The vacuum layer with the thickness of 10 Å was inserted to avoid interactions between two slabs. The supercell contained eight crystal units and eight atom layers with 16 Bi atoms, 8 W atoms, and 48 O atoms. To simulate the actual surface of the Bi_2WO_6 bulk, the top four layers of W and O atoms were relaxed and the bottom four layers of Bi and O atoms were fixed in all geometry optimization. All calculations were performed using Perdew-Burke-Ernzerhof (PBE) functional within the generalized gradient approximation (GGA) in Dmol^3 program embedded in Materials Studio 7.0 software.[2-5] Because H_2O adsorption on the surface involves noncovalent forces, such as hydrogen bonding and van der Waals interactions, dispersion correction for density functional theory (DFT) was performed using Ortmann-Bechstedt-Schmidt (OBS) method.[6] Due to the relativistic effects of Bi and W elements, all electron relativistic method was adopted to treat core electrons.[7, 8] The basis set version 4.4 and the double-numeric basis plus polarization function (DNP) were used. The global real space orbital cutoff of atomic basis set was set to be 4.0 Å. The convergence criteria for geometry optimization and energy calculation were 2×10^{-5} Hartree for energy, 4×10^{-3} Hartree/Å for maximum force, 5×10^{-3} Å for maximum displacement, and 1.0×10^{-5} Hartree for the self-consistent field.[9]

In Bi_2WO_6 crystal, W central atom is coordinated with six ligands of O atoms, which present a tetragonal bipyramidal structure. Similarly, the perfect Bi_2WO_6 surface also has similar octahedral structure, shown in Fig. S1. As an adsorbate, H_2O can be easily adsorbed on Bi_2WO_6 surface

through hydrogen bonding interaction between O atom on the top site and H atom of H_2O. The adsorption energy (E_{ad}) can be defined as

$$E_{ad} = E_{water} + E_{surface} - E_{complex}$$

Where E_{water}, $E_{surface}$, and $E_{complex}$ represent the energies of the water, surface, and adsorption complex between water and surface, respectively. As shown in Fig. S1c, one H_2O molecule can form two hydrogen bonds with two surrounding O atoms on the surface, in which the adsorption energy is 14.5 kcal/mol. When water exits on then Bi_2WO_6 surface with O vacancy (Fig. S1b), one H_2O molecule can occupy the O vacancy and be strongly adsorbed on the surface through coordination with surface W atom (Fig. S1d). The adsorption energy (E_{ad}) is up to 29.5 kcal/mol, which is larger than that on the perfect surface. Therefore, O vacancy can promote H_2O adsorption on the Bi_2WO_6 surface, which is beneficial for enhancing the OER activity of the catalysts.

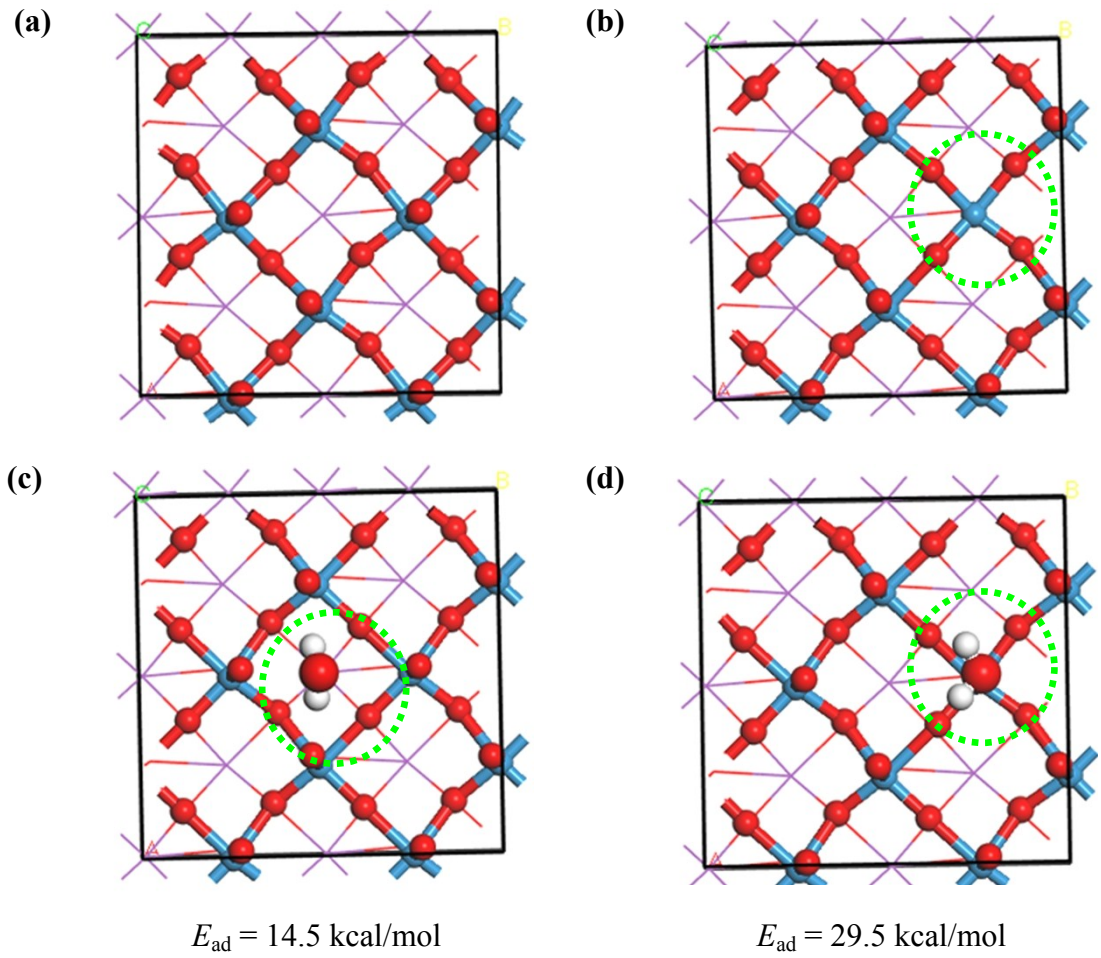

Fig. S1 (a) Perfect Bi_2WO_6 surface, (b) Bi_2WO_6 surface with one O vacancy, (c) H_2O adsorption on perfect Bi_2WO_6 surface, and (d) H_2O adsorption on Bi_2WO_6 surface with one O vacancy.

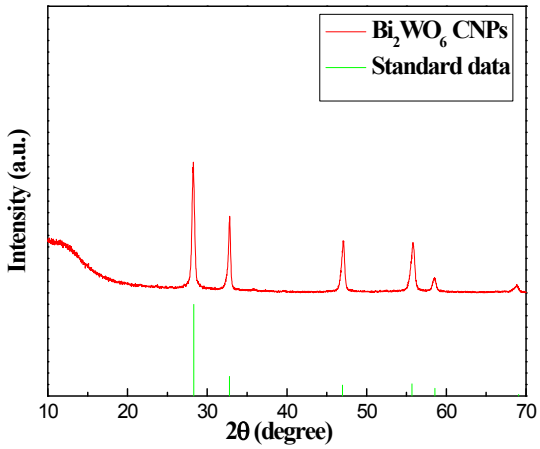

Fig. S2 XRD pattern of the synthesized Bi_2WO_6 CNPs (a). Standard data obtained from JCPDS No. 73-1126 (b).

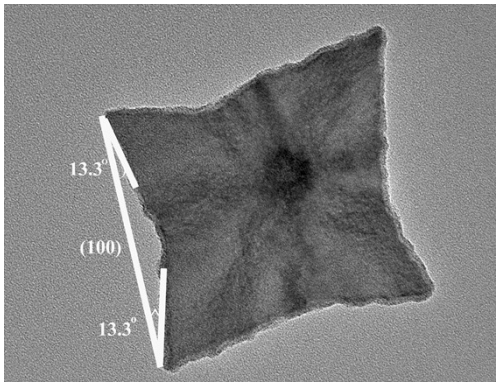

Fig. S3 A typical TEM image of Bi_2WO_6 CNP.

By carefully measuring the TEM image (Fig. S3), the angles between the concave facets and the (100) facets are about 13.3°. To an orthorhombic system, the angle (θ) between two different crystal planes can be calculated by the formula below:

$$\cos\theta = \frac{\frac{h_1h_2}{a^2} + \frac{k_1k_2}{b^2} + \frac{l_1l_2}{c^2}}{\sqrt{\left(\frac{h_1^2}{a^2} + \frac{k_1^2}{b^2} + \frac{l_1^2}{c^2}\right)\left(\frac{h_2^2}{a^2} + \frac{k_2^2}{b^2} + \frac{l_2^2}{c^2}\right)}}$$

Where θ = 13.3°, a = 5.457, b = 5.436 , c = 16.427 , h_1 =1, k_1 = 0, l_1 = 0

As a result, $$0.973 = \frac{\frac{h_2}{a^2}}{\sqrt{\frac{1}{a^2}(\frac{h_2^{\ 2}}{a^2} + \frac{k_2^{\ 2}}{b^2} + \frac{l_2^{\ 2}}{c^2})}}$$

$$h_2^{\ 2} = 19k_2^{\ 2} + 2l_2^{\ 2}$$

$$\because h_2, k_2, l_2 \text{ are integers}$$

$$\because l_2^{\ 2} = \frac{h_2^{\ 2} - 19k_2^{\ 2}}{2} \geq 0$$

$$If\ k_2 \neq 0, then\ h_2 \geq \sqrt{19}k_2$$

The least h_2 value is 5 in order to meet the above conditions.

$$If\ k_2 = 0, then\ h_2 = \sqrt{2}l_2$$

In order to reduce the error of the equation solution, the least h_2 and l_2 values are 3 and 2, respectively. In either case, h_2 is bigger than 3. Therefore the as-obtained Bi_2WO_6 concave nanoplates contain high energy facets.

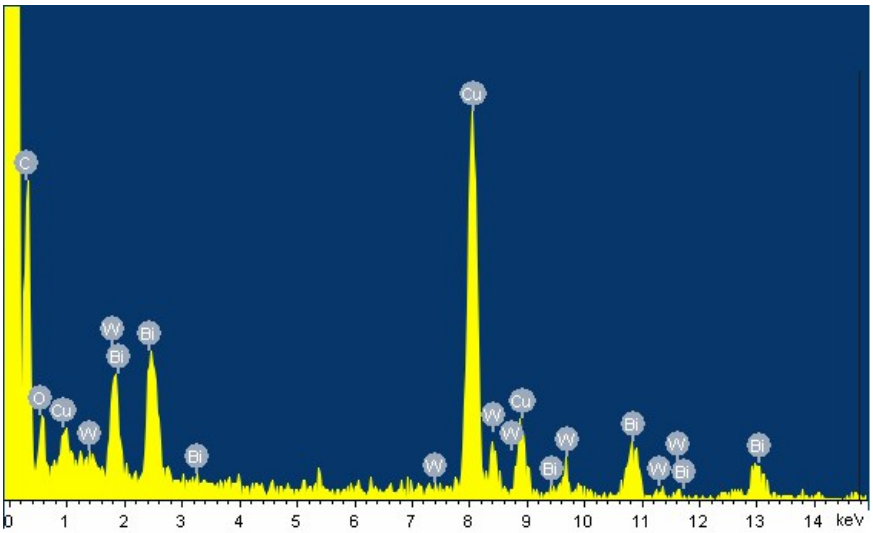

Fig. S4 EDX spectrum of the synthesized Bi_2WO_6 CNPs.

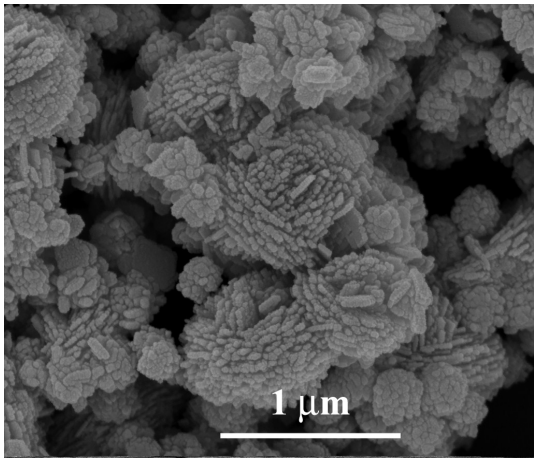

Fig. S5 FE-SEM image of the sample synthesized without use of oleylamine.

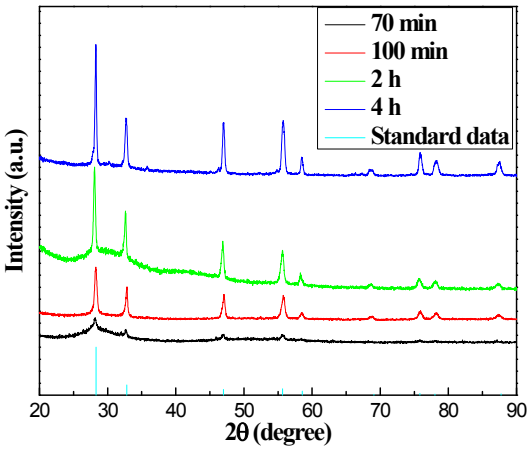

Fig. S6 XRD patterns of the intermediates.

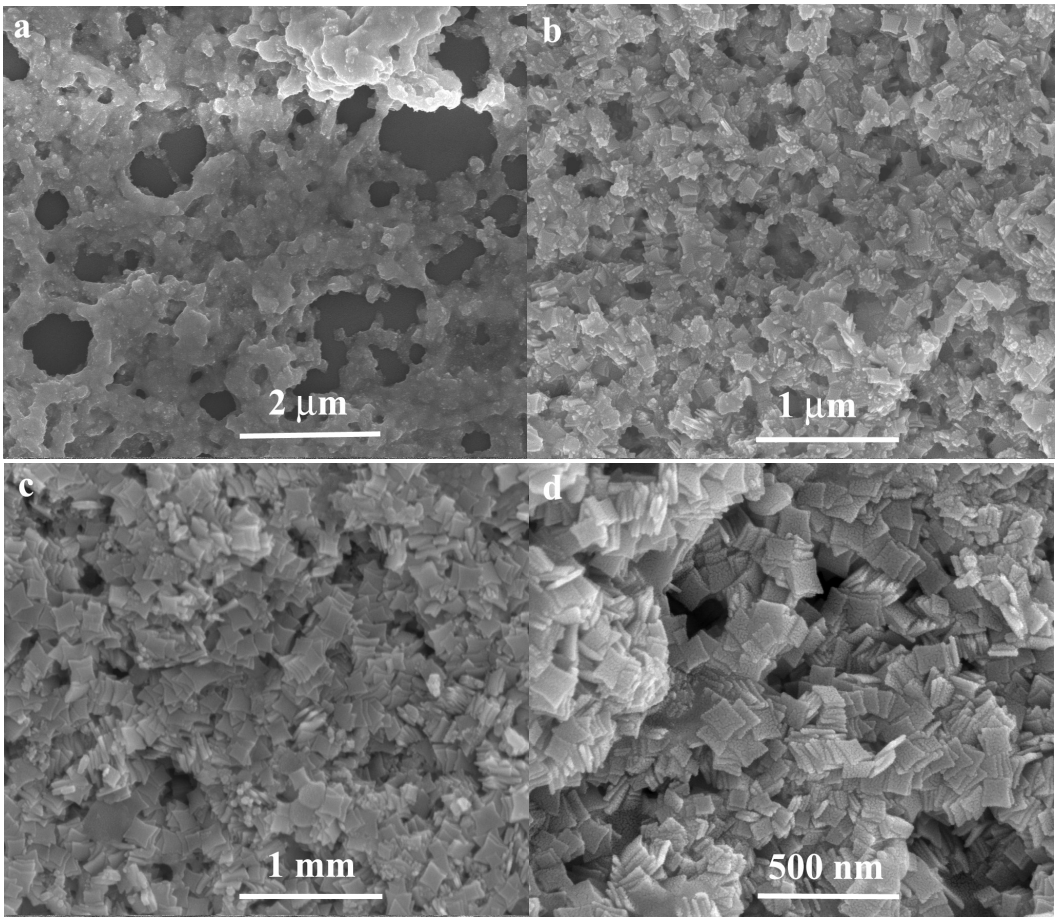

Fig. S7 FE-SEM images of the intermediates obtained at different reaction stages: 70 min (a), 100 min (b), 2 h (c), and 4 h (d).

Fig. S6 represents the XRD patterns of the samples synthesized for 70 min, 100 min, 2 h, and 4 h, respectively. As shown in Fig. S6, the crystal phase of Bi_2WO_6 has been produced within initial 70 min. With prolonged solvothermal treatment time, the crystallinity of Bi_2WO_6 products was further improved, judging from the increase of absolute intensities of all the diffraction peaks. SEM observations show that the intermediates were irregular nanoparticles (70 min), a small quantity of Bi_2WO_6 CNPs and irregular nanoparticles (100 min), small Bi_2WO_6 CNPs and big Bi_2WO_6 CNPs (2 h), and uniform Bi_2WO_6 CNPs (4 h), respectively. Therefore the formation of Bi_2WO_6 CNPs went through anisotropic growth of nanoparticles into concave nanoplates because of selective adsorption of oleylamine and Ostwald ripening process of concave nanoplates (large Bi_2WO_6 CNPs grow at the expense of small Bi_2WO_6 CNPs). .

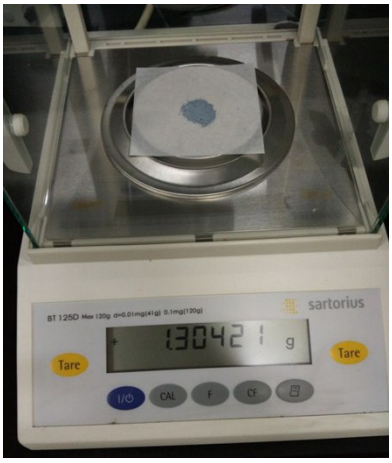

Fig. S8 Digital photo of the sample obtained through one-pot reaction.

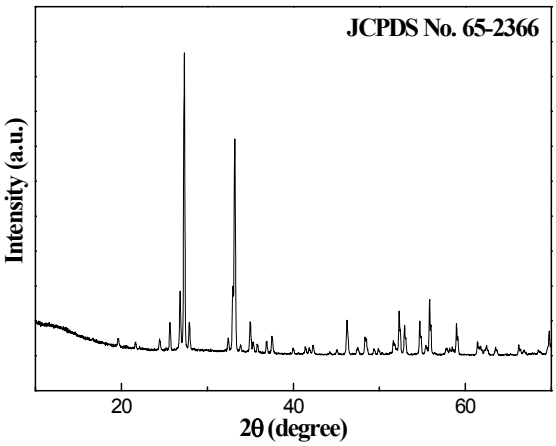

Fig. S9 XRD pattern of rod-like Bi_2O_3.

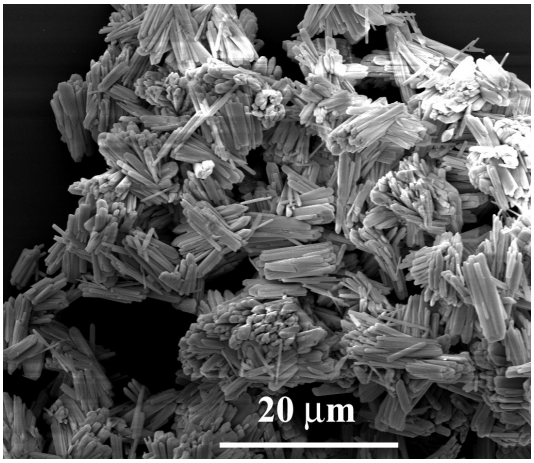

Fig. S10 FE-SEM image of the synthesized Bi_2O_3.

All diffraction peaks in Fig. S9 can be indexed to pure monoclinic-phase Bi_2O_3 (JCPDS No. 65-2366). As can be seen from Fig. S10, the products take on rod-like appearance.

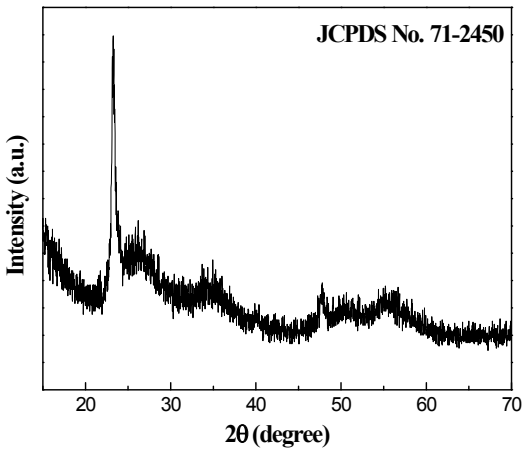

Fig. S11 XRD pattern of $W_{18}O_{49}$ nanowires.

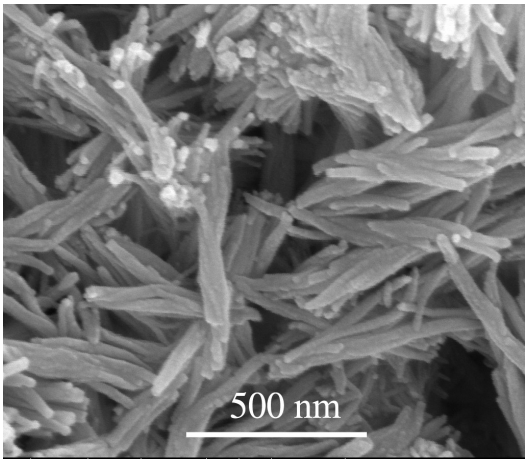

Fig. S12 FE-SEM image of the synthesized $W_{18}O_{49}$.

All diffraction peaks in Fig. S11 can be indexed to pure monoclinic-phase $W_{18}O_{49}$ (JCPDS No. 71-2450). As can be seen from Fig. S12, the products are nanowires.

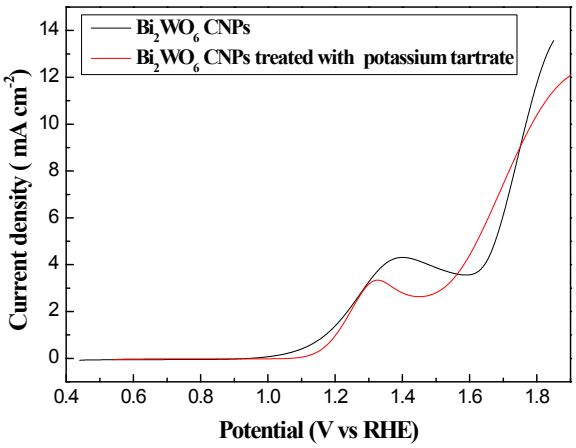

Fig. S13 LSV curves of Bi_2WO_6 CNPs and Bi_2WO_6 CNPs treated with potassium tartrate.

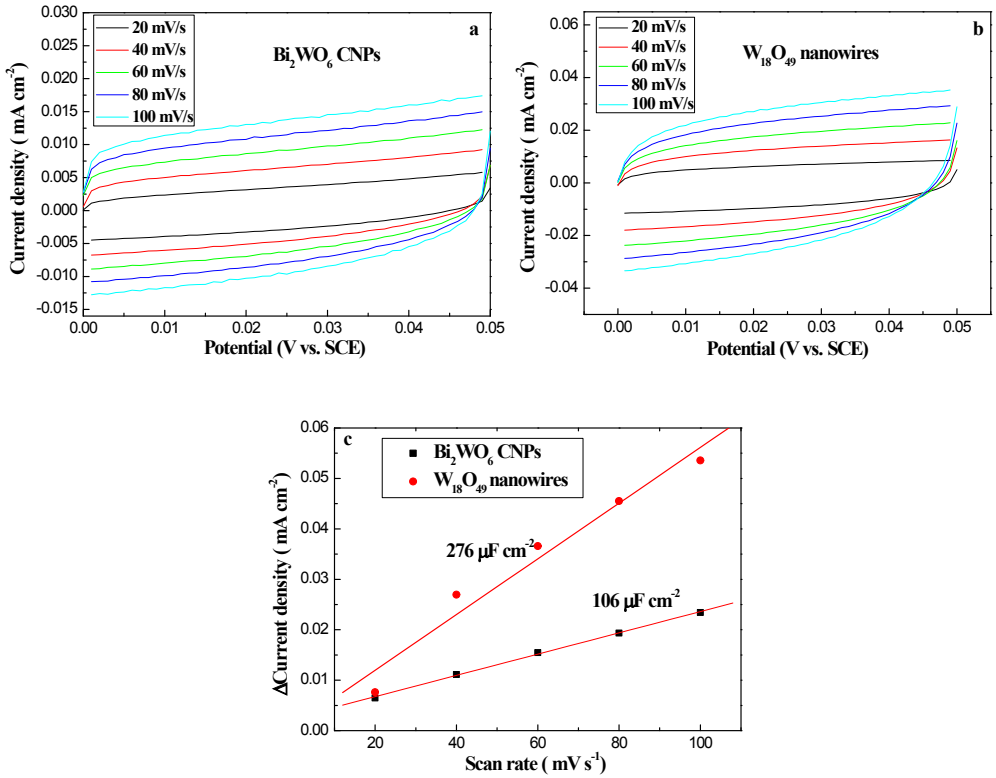

Fig.14 CV curves of Bi_2WO_6 CNPs (a) and $W_{18}O_{49}$ nanowires (b). Charging current density differences plotted against scan rates for Bi_2WO_6 CNPs and $W_{18}O_{49}$ nanowires (c).

Fig. 14a and 14b represent CV curves of Bi_2WO_6 CNPs and $W_{18}O_{49}$ nanowires at different scan rates (from 20 to 100 mV s^{-1} in 20 mV s^{-1} increments) performed in a potential range in which no faradic processes were observed. The corresponding capacitive currents density at 0.025 V versus SCE are plotted as a function of scan rate, respectively. The results show that the current density has good linear relationship with the scan rate for the two materials, which is consistent with capacitive charging behavior. The linear slope obtained by fit is equivalent to twice of the double-layer specific capacitance. As a result, the specific capacitance of $W_{18}O_{49}$ nanowires (276 μF cm^{-2}) is about 2.6-times larger than that of Bi_2WO_6 CNPs (106 μF cm^{-2}).

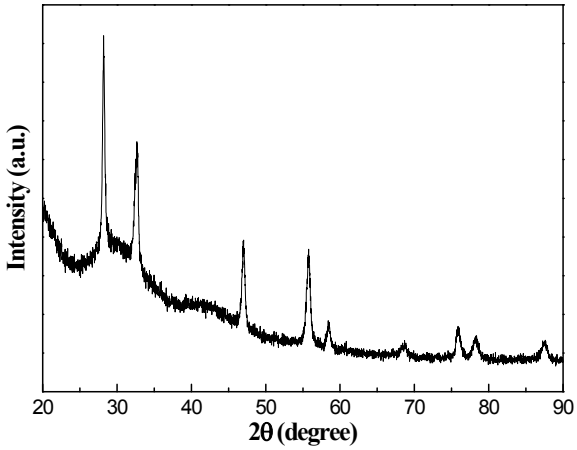

Fig. S15 XRD pattern of the synthesized Bi_2WO_6 nanoplates.

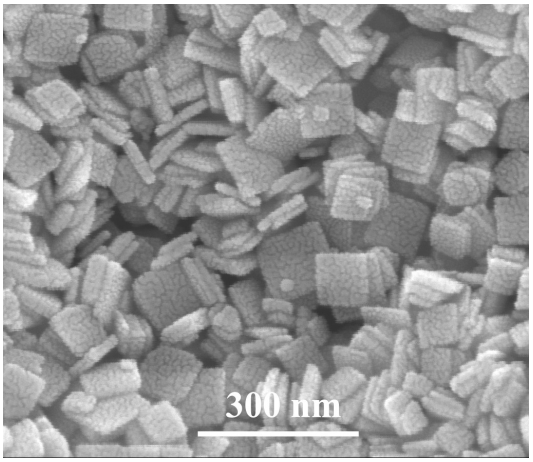

Fig. S16 FE-SEM image of the synthesized Bi_2WO_6 nanoplates.

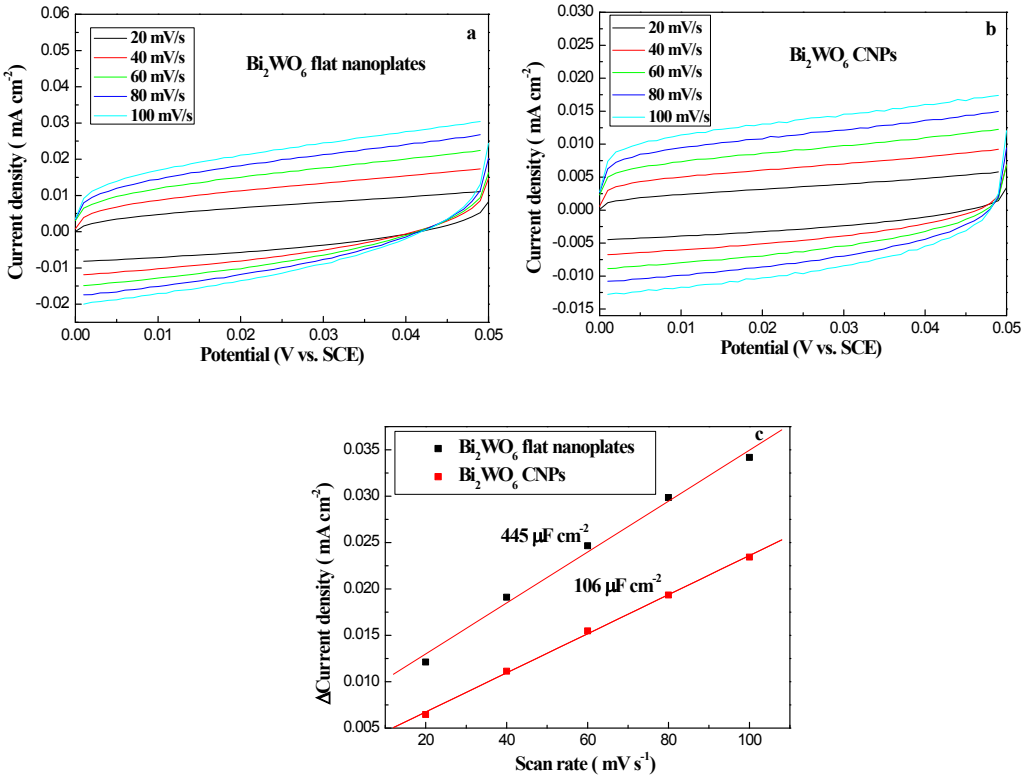

Fig.17 CV curves of Bi_2WO_6 flat nanoplates (a) and Bi_2WO_6 CNPs (b). Charging current density differences plotted against scan rates for Bi_2WO_6 CNPs and Bi_2WO_6 flat nanoplates (c).

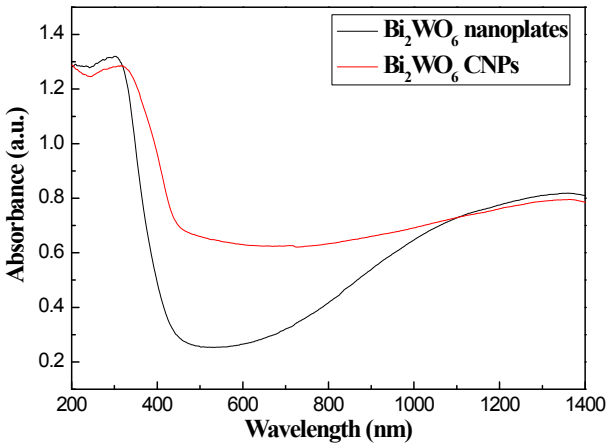

Fig. S18 UV-visible diffuse reflectance spectra of Bi_2WO_6 nanoplates and Bi_2WO_6 CNPs after treated with 40 mL of H_2O_2 (60 mg/mL).

Table S1. OER activities of some typical inorganic electrocatalysts under neutral conditions

Material	**Onset potential (V)**	**Current density (mA cm^{2-}) at η = 0.54 V**	**Reference**
Co-Pi	0.28	1.62	13
Co_3O_4/SWNTs	0.38	2.42	14
δ-MnO_2	0.60	0.22	15
$Co(PO_3)_2$	0.31	1.04	16
ZrS_3 nanosheets	0.61	0.02	17
$Mn_3(PO_4)_2{\cdot}3H_2O$	0.45	0.03	18
Mo_5O_8 nanoparticles	0.44	0.46	19
Co_3S_4 nanosheets	0.31	2.02	20
Bi_2WO_6 nanoplates	0.37	10 .00	This work

References

1. Wolfe, R.W.; Newnahm, R. E.; Kay, M. I. *Solid State Commun.* **1969**, *7*, 1797.
2. Perdew, J. P.; Burke, K.; Ernzerhof, M. *Phys. Rev. Lett.* **1996**, *77*, 3865.
3. Delley, B. *J. Chem. Phys.* **1990**, *92*, 508.
4. Delley, B. *J. Chem. Phys.* **2000**, *113*, 7756.
5. Accelrys Inc., DMol^3 program in *Materials Studio 7.0*, 2014.
6. Ortmann, F.; Bechstedt, F.; Schmidt, W. G. *Phys. Rev. B* **2006**, *73*, 205101.
7. D. Koelling, D.; Harmon, B. N. *J. Phys. C: Solid State Phys.* **1977**, *10*, 3107.
8. Douglas, M.; Kroll, N. M. *Ann. Phys. (San Diego)* **1974**, *82*, 89.
9. Fang, G. Y.; Ma, J. *Nanoscale* **2013**, *5*, 11856.
10. Wu, Y. Q.; Lu, G. X. *Phys. Chem. Chem. Phys*. **2014**, *16*, 4165.
11. Xi, G. C.; Ou, S. X.; Li, P.; Ye, J. H.; Ma, Q.; Su, N.; Bai, H.; Wang, C. *Angew. Chem. Int. Ed.* **2012**, *51*, 2395.
12. Zhou, Y.; Tian, Z. P.; Zhao, Z. Y.; Liu, Q.; Kou, J. H.; Chen, X. Y.; Gao, J.; Yan, S. C.; Zou, Z. G. *ACS Appl. Mater. Interfaces* **2011**, *3*, 3594.
13. Kanan, M.W.; Nocera, D.G. *Science* **2008**, 321, 1072.

14. Wu, J.; Xue, Y.; Yan, X.; Yan, W.; Cheng, Q.; Xie, Y. *Nano Res.* **2012**, *6*, 521.

15. Takashima, T.; Hashimoto, K.; Nakamura, R. *J. Am. Chem. Soc.* **2012**, *134*, 1519.

16. Ahn, H. S.; Tilley, T. D. *Adv. Funct. Mater.* **2013**, *23*, 227.

17. Xie, J.; Wang, R.; Bao, J.; Zhang, X.; Zhang, H.; Li, S.; Xie, Y. *Inorg. Chem. Front.* **2014**, *1*, 751.

18. Jin, K.; Park, J.; Lee, J.; Yang, K. D.; Pradhan, G. K.; Sim, U.; Jeong, D.; Jang, H. L.; Park, S.; Kim, D.; Sung, N. E.; Kim, S. H.; Han, S.; Nam, K. T. *J. Am. Chem. Soc.* **2014**, *136*, 7435.

19. Jeong, D.; Jin, K.; Jerng, S. E.; Seo, H.; Kim, D. Nahm, S. H.; Kim, S. H.; Nam, K. T. *ACS Catal*. **2015**, *5*, 4624.

20. Liu, Y. W.; Xiao, C.; Lyu, M. J.; Lin, Y.; Cai, W. Z.; Huang, P. C.; Tong, W.; Zou, Y. M.; Xie, Y. *Angew. Chem. Int. Ed*. **2015**, *54*, 11231.